Isogeometric Framework for Aeroelastic Wind Turbine Rotor Analysis

Etana.Ferede[1], Mostafa.M. Abdalla[1], and Johannes K.S. Dillinger[2]

[1] Delft University of Technology
Kluyverweg 1, Delft,The Netherlands
E.A.Ferede@tudelft.nl
[2] German Aerospace Center(DLR)
Bunsenstrasse 10, Gottingen, Germany

Keywords: Wind turbine, Isogeometric, Aeroelasticity, Multi-Fidelity, Composite, Optimization

Abstract: An isogeometric framework is presented for parametrizing a wind turbine rotor blade and analysing its response. The framework consists of multi-fidelity approach for wind turbine rotor analysis. The aeroelastic loads are determined using a low-fidelity model. This low-fidelity model is based on isogeometric approach to model both the structural and aerodynamic properties, because of its suitability for shape and size optimization. The structural properties are determined using a geometrically exact beam model and a standard Blade Element Momentum(BEM) method is used to calculate the aerodynamic loads. In addition, the aerodynamic loads calculated using BEM theory are modified to account for change in the blade shape during shape optimization or for very flexible blade undergoing large deformation. The cross-sectional properties of the blade, needed for the beam model, are determined using an in-house tool that generates the cross-sectional stiffness properties with all possible couplings for thin-walled, multi-cell, open or closed cross-sections with anisotropic properties. The aeroelastic loads are applied in finite element analysis (Nastran) as static loads to a shell model of the blade; and both the stress response and buckling response are extracted. In addition, sensitivity coefficients of the aeroelastic responses to the design variables are calculated, such that this framework can also be used to optimize the rotor blade. Furthermore, the capabilities of Nastran are extended such that design dependent loads can be applied, resulting in correct aeroelastic sensitivities of Nastran responses. The framework is verified against results from the commercial codes *FAST* and *GH Bladed*, using the NREL $61.5m$ rotor blade as a baseline for comparison,showing good agreement. Finally, the capability of the present method in designing and analysing non-conventional blades is demonstrated by investigating the aeroelastic characteristics of the curved Sandia $30m$, *STAR* blade.

1. INTRODUCTION

Wind turbines are designed for increased energy yield while minimizing operational cost, as to make it competitive with other energy sources. In the past decade an increasing number of wind farms has been installed offshore, while the size of HAWTs has also steadily increased [1]. However, larger HAWT rotor blades are more flexible, which means aeroelasticity needs to be taken into account.

Several aeroelastic codes for wind turbine analysis have been developed. Most approaches[2, 3, 4, 5, 6] use Blade Element Momentum(BEM) theory for calculating the aerodynamic loads, while the structural models are based either on FEM, modal approach or Multi-body dynamics. A detailed review on wind turbine aeroelasticity can be found in [7].

Furthermore, the increased cost of energy production, necessitates the design of more efficient wind turbine rotor blades. Many researches are continuously being conducted to design wind turbine rotor blades with increased energy yield, while minimizing the cost. Several optimization methods[8, 9, 10, 11] have been proposed to minimize the Cost Of Energy(COE) of HAWTs, that did not incorporate the aeroelastic effect of wind turbine blades. However, as wind turbine rotor blades became more flexible, their aeroelastic effect is being incorporated during the optimization process [12, 13, 14, 15]. In addition,the use of bend-twist coupling in wind turbine blades is increasingly being investigated for increased energy capture or for load reduction [16, 17]. Bend-twist coupling in blades can be achieved by optimizing the fibre orientations

of the composite laminates [18] or designing a swept blade planform [19], where the additional moment caused by the blade sweep twists the blade to stall or to feather depending on the direction of the blade sweep.

The demand for designing an optimal wind turbine rotor blades(in terms of planform or material distribution), places a premium on rotor blade optimisation. A general framework is presented in this work that is capable of parametrizing efficiently a wind turbine rotor blade in terms of its geometry and material, i.e planform, beam axis(as to design curved blades) and laminate thickness together with the fibre angles of a composite material. The framework is also be capable of including static aeroelastic effect during analysis. This allows the user to investigate the effect of changing different parameters of the rotor blade on the wind turbine rotor performance, making the design or optimization of a blade, using both the geometry and material as design variables, more efficient.

NURBS representations are commonly used to construct Computer Aided Design (CAD) descriptions of engineering products. More recently the same NURBS representations are used to model physical response quantities both in structural analysis [20], where they are used to describe the variation of displacements and/or stresses, and in aerodynamic analysis where it is used to describe the variation of flow velocities and pressure [21]. The use of the same description for both geometry and physics is termed isogeometric analysis (IGA). In this paper, we create an IGA based framework not only for describing the geometry of wind turbine rotor blades and analysing their response, but also as means for structural and aerodynamic design parametrisation.

The rest of this paper is organised as follows: the first section gives a brief overview of NURBS and their properties used in the present framework. Followed by a section describing the parametrization of a wind turbine rotor blade used in current framework. The aeroelastic model that describes the structural and aerodynamic models, together with the centrifugal loads is described afterwards. Finally, the aeroelastic model is verified in the result section using the NREL $61.5m$ rotor blade [22] as a baseline for comparison. The capability of the present method in designing and analysing non-conventional blades is demonstrated by investigating the aeroelastic characteristics of the Sandia $30m$, *STAR* blade [23].

2. NURBS GEOMETRY AND PROPERTIES

One-dimensional B-splines are defined over an interval on the real axis described by a *knot vector* $\boldsymbol{\Xi}$

$$\boldsymbol{\Xi} = \left\{\xi_1 = ... = \xi_{p+1} = 0, \xi_{p+2}, ..., \xi_n, \xi_{n+1} = ... = \xi_{n+p+1} = 1,\right\}, \xi_1 \leq \xi_2 \leq \ldots \leq \xi_{n+1}, \tag{1}$$

where $\boldsymbol{\Xi}$ in this case is an open *knot vector*. The B-splines of degree p are defined recursively as,

$$N_{i,0}(\xi) = \begin{cases} 1 & \text{if } \xi_i \leq \xi < \xi_{i+1} \\ 0 & \text{otherwise} \end{cases} \quad \text{and,} \tag{2}$$

$$N_{i,p}(\xi) = \frac{\xi - \xi_i}{\xi_{i+p} - \xi_i} N_{i,p-1}(\xi) + \frac{\xi_{i+p+1} - \xi}{\xi_{i+p+1} - \xi_{i+1}} N_{i+1,p-1}(\xi). \tag{3}$$

The knot vector has $n + p + 1$ elements where n is the number of non-zero intervals $[\xi_i, \xi_{i+1})$ called a *knot span*. For the present method, the basis functions are C^{∞} continuous in the interior of the knot span and C^{p-1} continuous at boundary of the knot span. Detailed description on B-spline functions can be found in [24].

The pth degree Non-Uniform Rational B-Spline(NURBS) is a piecewise rational function defined by the projective transformation,

$$R_{i,p}(\xi) = \frac{N_{i,p}(\xi) w_i}{\omega(\xi)}, \tag{4}$$

where w_i is a positive weight factor of the spline function $N_{i,p}(\xi)$. The denominator of equation 4 is referred to as weighting function, i.e.

$$\omega(\xi) = \sum_{i=1}^{n} N_{i,p}(\xi) w_i. \tag{5}$$

The continuity properties of the B-spline functions carry over to NURBS functions. B-spline may be recovered from NURBS by assigning uniform weights to all basis functions. The additional freedom in choice of weights make NURBS representations more versatile than B-splines. Moreover, common geometric shapes such as conic sections are exactly representable using NURBS.

Some of the characteristic features of B-splines and NURBS is illustrated in figure 1, where the basis functions of B-splines and NURBS are plotted for $p = 3$ and $\boldsymbol{\Xi} = \left\{0, 0, 0, \frac{1}{4}, \frac{1}{2}, \frac{3}{4}, 1, 1, 1\right\}$.

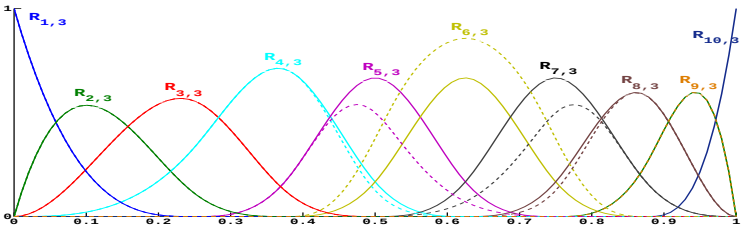

Figure 1. Cubic basis functions of B-splines and NURBS. The solid lines represent the B-spline basis $N_{i,3}$ with $i = 1, \ldots, n$, whereas modifying a single weight($w_7 = 2$) results in $p + 1$ rational basis functions $R_{i,3}$ with $i = 4, \ldots, 7$, represented by dashed lines. All other basis functions are unaffected.

2.1. NUBRS curves

A B-spline curve is a linear combination of B-spline functions and control points in $\mathbb{R}^d$ [24]. The position vector of a point on the curve is given by,

$$\boldsymbol{r}(\xi) = \sum_{i=1}^{n} N_{i,p}(\xi)\boldsymbol{P}_i. \tag{6}$$

The control points $\boldsymbol{P}_i$, form the so-called control polygon.

A d-dimensional NURBS curve is obtained by projecting a $d + 1$ dimensional B-spline curve []. The control points of the B-spline curve, denoted by $\boldsymbol{P}^w$, are referred to as homogeneous coordinates. The projected control points, denoted by $\boldsymbol{P}$, are referred to as non-homogeneous control points. The $d + 1$ component of the corresponding B-spline curve is the control point weight.

A NURBS curve generated by an open knot vector is tangent to the control polygon at either end. An affine transformation may be applied to a NURBS curve by applying it to the control points. Because the NURBS shape functions have local support, change of a control point $\boldsymbol{P}_i$ or its weight w_i results only in local change of the NURBS curve.

2.2. Knot refinement

Knot refinement gives flexibility for the proposed framework to have different level of parametrization while preserving the geometry. The coarse knot vector for instance is used to define the geometric properties of the structure and, the refined knot vector is used for analysis, in which large number control points are needed to get converged result, making this method particularly useful for optimization.

Knot refinement is the application of multiple *knot insertion* simultaneously. For *Knot insertion*, a single knot $\bar{\xi} \in [\xi_k, \xi_{k+1})$ is added to the knot vector Ξ, resulting in the extended knot vector $\Xi \subset \hat{\Xi}$. As a result, the number of basis functions is increased by one, i.e. $\bar{n} = n + 1$. *Knot insertion* changes the vector space of the basis function while preserving the geometry [], i.e.

$$\sum_{i=1}^{n} N_{i,p}(\xi)\boldsymbol{P}_i^w = \sum_{j=1}^{\bar{n}} \bar{N}_{i,p}(\xi)\bar{\boldsymbol{P}}_j^w, \tag{7}$$

where $\bar{\boldsymbol{P}}_j^w$ is an arbitrary homogeneous control point in the new control polygon, calculated from the old control polygon as

$$\bar{\boldsymbol{P}}_j^w = \alpha_i \boldsymbol{P}_i^w + (1 - \alpha_i)\boldsymbol{P}_{i-1}^w, \tag{8}$$

where the definition of the parameter α_i is given in [24].

Assuming that the old knot vector Ξ is extended with r new knots, the *knot refinement* may be expressed in matrix form as

$$\bar{\boldsymbol{P}}^w = \boldsymbol{\mathcal{L}}\boldsymbol{P}^w, \tag{9}$$

where $\boldsymbol{P}^w$ and $\bar{\boldsymbol{P}}^w$ are matrix representation of the coarse and refined (homogeneous)control points, respectively. The columns of $\boldsymbol{P}^w$ and $\bar{\boldsymbol{P}}^w$ are the components of a single control point. The symbol $\boldsymbol{\mathcal{L}}$ is a banded matrix of size $(n + r \times n)$ containing information on the knot refinement. Efficient method of performing knot refinement without inserting knots sequentially, using equation 8, is discussed extensively in [25].

The refined non-homogeneous control points $\bar{\boldsymbol{P}}_j$ are related to the coarse non-homogeneous control points $\boldsymbol{P}_i$ as

$$\bar{\boldsymbol{P}} = \boldsymbol{\mathcal{L}}_w\boldsymbol{P}, \tag{10}$$

where

$$\boldsymbol{\mathcal{L}}_w = \bar{\boldsymbol{W}}^{-1}\boldsymbol{\mathcal{L}}\boldsymbol{W}, \tag{11}$$

and $\boldsymbol{P}$ and $\bar{\boldsymbol{P}}$ are matrix representation of the coarse and refined (non-homogeneous)control points, respectively. The diagonal matrix $\boldsymbol{W}$ contains the weights w_i, with $i = 1, \ldots, n$, for control points $\boldsymbol{P}$, whereas $\bar{\boldsymbol{W}}$ contains the weights w_j, with $j = 1, \ldots, n + r$, for control points $\bar{\boldsymbol{P}}$.

3. PARAMETRIC BLADE MODEL GENERATION

A parametric approach is set-up capable of modelling wind turbine blades with generic shapes like sweep, curvature or any other complex shapes. The parametrization of the current method allows for parametric study or shape optimization routine, where the shape of the blade and material properties can easily be varied.

The blade geometry is modelled with respect to the rotating frame denoted by (X,Y,Z), shown in figure 2. The base vector $\boldsymbol{e}_3$ is orthogonal to the rotor plane, while $\boldsymbol{e}_1$, $\boldsymbol{e}_2$ span the rotor plane. The aerodynamic module accounts for wind shear, where the aerodynamic loads are calculated at azimuth position ϕ(see figure 2).

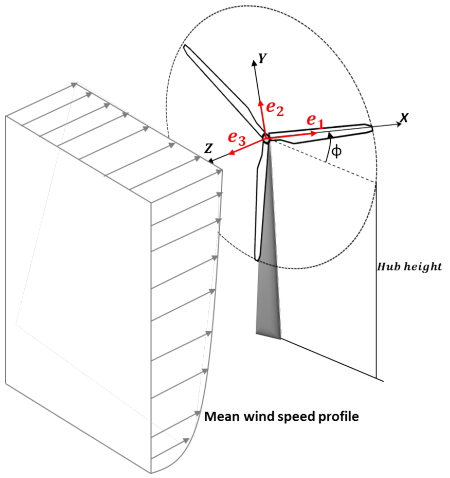

Figure 2. Definition of moving reference frame and wind shear for wind turbine aeroelastic analysis

The present method makes use of the NURBS function, described in section 2, to generate the blade shape and material properties. Multi level discretization scheme is used to parametrize the geometry and material with different set of control points as shown in figure 3. The control point properties of the geometry and material are mapped unto the analysis space using the *Knot refinement* method described in sub-section 2.2.

3.1. Geometry model

The geometry of a wind turbine blade may be defined as a series of cross-sections connected by a beam axis. The beam axis is parametrized with a set of position vectors defining the beam axis $\boldsymbol{P}_r$, while a cross-section is parametrized with: a set of airfoil shapes $\boldsymbol{P}_{paf}$, and the corresponding weights $\boldsymbol{C}$, a set of twist distribution $\boldsymbol{P}_\theta$, intersection point of the beam axis with the cross-sectional plane $\boldsymbol{P}_\alpha$, and spar locations on the unit chord line $\boldsymbol{V}_s$.

Beam axis

The beam axis is interpolated using the NURBS function and the control point values of the beam axis as,

$$\boldsymbol{r}_b(\xi) = \sum_{i=1}^{n} R_{i,p}(\xi)\boldsymbol{P}_{\boldsymbol{r}i}, \tag{12}$$

where $\boldsymbol{P}_{\boldsymbol{r}i}$ is the position vector of the beam axis at control point i.

The arch-length, which is the distance from the root of the blade till the parametric point ξ, is given by,

$$s(\xi) = \int_0^{\xi} J(\xi)d\xi, \tag{13}$$

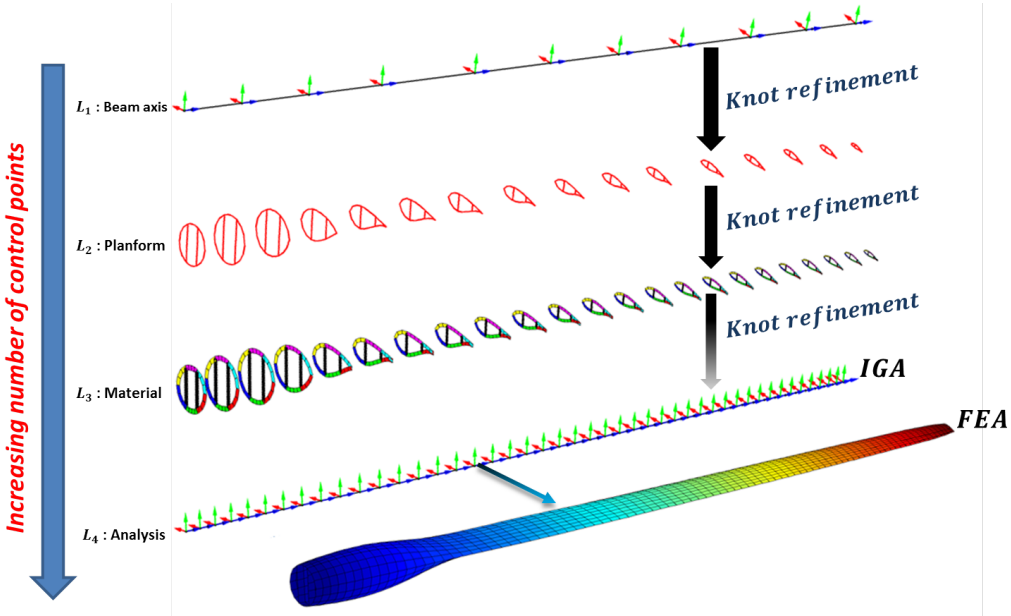

Figure 3. Multi level parametrization of a wind turbine blade

where $J(\xi)$ is the Jacobian, defined as,

$$J(\xi) = \left\| \frac{d\boldsymbol{r}_b}{d\xi} \right\|. \tag{14}$$

The definition of the arc length, given in equation 13, is used in subsection 3.3 to generate the finite element model.

The cross-sections are orthogonal to the beam axis. Consequently, the body attached base vector normal to the cross-section is tangent to the beam axis, i.e.

$$\boldsymbol{g}_1 = \frac{1}{J(\xi)} \frac{d\boldsymbol{r}_b}{d\xi}. \tag{15}$$

The remaining two, body attached, base vectors($\boldsymbol{g_2}, \boldsymbol{g_3}$) span the plane of the cross-section, calculated as

$$\tilde{\boldsymbol{g}}_2(\xi) = \boldsymbol{g}_1(\xi) \times \boldsymbol{e}_2 \qquad \text{and} \qquad \tilde{\boldsymbol{g}}_3(\xi) = \tilde{\boldsymbol{g}}_2(\xi) \times \boldsymbol{g}_1(\xi), \tag{16}$$

where $\boldsymbol{e}_2$ is a base vector of the rotating coordinate system(see figure 2).

The base vector tangent to the beam axis($\boldsymbol{g}_1$) remains unaffected by the structural twist $\theta(\xi)$, while $\boldsymbol{g_2}$ and $\boldsymbol{g_3}$ are rotated, such that

$$\boldsymbol{g}_2(\xi) = cos(\theta)\tilde{\boldsymbol{g}}_2 - sin(\theta)\tilde{\boldsymbol{g}}_3 \qquad \text{and} \qquad \boldsymbol{g}_3(\xi) = sin(\theta)\tilde{\boldsymbol{g}}_2 + cos(\theta)\tilde{\boldsymbol{g}}_3, \tag{17}$$

where $\theta(\xi)$ is the structural twist calculated using the twist distribution per control point and the NURBS function as,

$$\theta(\xi) = \sum_{i=1}^{n} R_{i,p}(\xi) \boldsymbol{P}_{\theta,i}, \tag{18}$$

where $\boldsymbol{P}_{\theta,i}$ is the ith control point value of the twist distribution. The base vectors spanning a cross-section at ξ are given in a matrix form as, $\boldsymbol{\Lambda}_0(\xi) = \left[\boldsymbol{g}_1, \boldsymbol{g}_2, \boldsymbol{g}_3\right]$.

Cross-section

The cross-sectional shape of a turbine blade at the parametric point ξ is modelled using the set of airfoil shapes supplied by the user. First the non dimensional airfoils need to be discretized to get uniform discretization of the airfoil shapes, suitable for interpolation. The airfoil shapes are provided as a text file of non dimensional airfoil coordinates in 2D plane, which is not necessary of the same size for all airfoils. The top and bottom skin of an airfoil are discretized separately by

computing the step size in chord direction(y_{i+1}), such that

$$\begin{aligned} \min_{y_{i+1}} \quad & \left(\int_{y_i}^{y_{i+1}} \sqrt{1 + \left(\frac{dz(x)}{dy} \right)^2} dy - \Delta C \right)^2, \\ \text{s.t.} \quad & y_{i+1} \in [y_i, 1], \end{aligned} \tag{19}$$

is satisfied for $i = 1, \ldots, N_c + 1$, where N_c is the number of elements in chord direction, and $[y_1, y_{N_c+1}] = [0, 1]$. The gradient $\frac{dz(y)}{dy}$, is computed using finite difference. The minimization problem defined in equation 19 is solved using the *Matlab fminbnd* function for

$$\Delta C = \frac{1}{N_c}, \tag{20}$$

where N_c is a user supplied parameter.

The chord-wise position of the spars is defined in vector form as,

$$\boldsymbol{V}_{sp} = [a_i, \ldots, a_S], \tag{21}$$

where a_i is the location of the ith spar on the non-dimensional chord line, and S is the total number of spars. The present parametrization method has a limitation that the number of spars is constant along the span of the blade, which my not be the case for some wind turbine blades.

The spars are discretized in $N_{s,i}$ equidistant elements, where $N_{s,i} = \left(N_c l_i \right)_r$ with the subscript r denoting rounding to the nearest integer. l_i is the length of spar i, which is the length of a vertical line intersecting the outer contour of an airfoil at a_i. An example of the airfoil discretization scheme is shown in figure 4, where the chord is discretized in 15 elements.

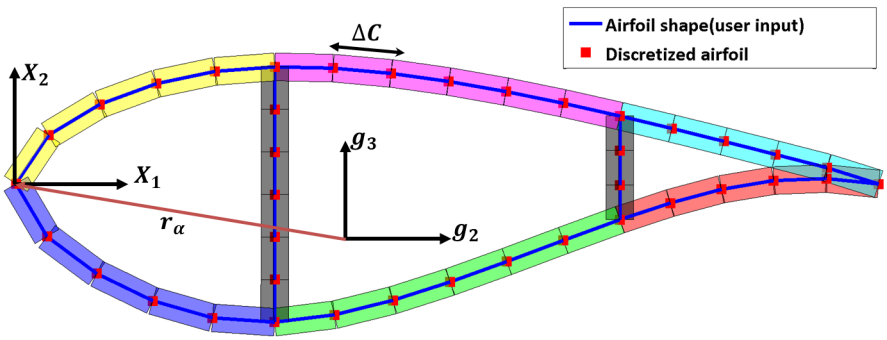

Figure 4. Example of airfoil discretization and property assignment on cross-section level, where each colour represents a single laminate. The local airfoil coordinates are denoted by $\boldsymbol{X}_1$ and $\boldsymbol{X}_2$, while $\boldsymbol{g}_2$ and $\boldsymbol{g}_3$ are the base vectors of the beam axis that span the cross-section.

The discretized airfoil shapes in a given pool are used to calculate the weighted airfoil shapes per control point. Weighted airfoil shapes are calculated as a linear combination of the airfoil shapes in a given pool(base airfoils) times user supplied weight factors, i.e.

$$\boldsymbol{P}_{af,i} = \sum_{j=1}^{m} C_{i,j} \boldsymbol{P}_{paf,j}, \tag{22}$$

where m is the number of base airfoils, $\boldsymbol{P}_{paf,j}$ is jth base airfoil shape, and $\boldsymbol{P}_{af,i}$ is a matrix representation of the weighted airfoil shape at control point i, where each row of $\boldsymbol{P}_{af,i}$ represent a point on the airfoil. The coefficient $C_{i,j}$ is a component of the $n \times m$ matrix $\boldsymbol{C}$ that contains the weights of the base airfoils per control point, and $\sum_{j=1}^{m} C_{i,j}$ is the chord length at control point i.

The shape of a cross-section in 2D is defined as,

$$\boldsymbol{R}_{2D}(\xi) = \boldsymbol{r}_\alpha + \sum_{i=1}^{n} R_{i,p}(\xi) \boldsymbol{P}_{af,i}, \tag{23}$$

where,

$$\boldsymbol{r}_\alpha = \sum_{i=1}^{n}\sum_{j=1}^{m} C_{i,j}\boldsymbol{P}_{\alpha,i}, \tag{24}$$

and $\boldsymbol{P}_{\alpha,i}$ is a non-dimensional vector at control point i defining the intersection of the beam axis with the cross-sectional plane(see figure 4). The 3D co-ordinate of a cross-section at ξ is given by,

$$\boldsymbol{R}_{3D,k}(\xi) = \boldsymbol{r}_b(\xi) + \boldsymbol{\Lambda}_0(\xi)\boldsymbol{R}_{2D,k}(\xi), \tag{25}$$

where the subscript k denotes a point on the cross-section.

3.2. Material properties

The present method uses composite materials to define the material properties of the wind turbine blade. The laminate properties used in the present method are comprised of: laminate thickness(h), membrane stiffness($\boldsymbol{A}$), and bending stiffness($\boldsymbol{D}$).

First the laminate properties per control point are determined by dividing the cross-section in $N_{pr}+1$ sections, where the contour of the cross-section is divided by N_{pr} sections(see figure 4). The length of each laminate, except the laminate for the shear webs, is defined by a non dimensional parameter describing the discretization of the (non-dimensional)chord for property assignment, i.e.

$$\boldsymbol{V}_{pr} = [0, a_1, \ldots, a_{N_{pr}-1}, 1], \tag{26}$$

where a_k with $k = 1, \ldots, N_{pr}+1$, is a partition point on the non-dimensional chord line, and $V_{pr,i+1} - V_{pr,i}$ is the length of a laminate projected on the non-dimensional chord. The laminate properties at ξ are calculated using the control point properties of the $N_{pr}+1$ laminates and the NURBS function as,

$$h^k(\xi) = \sum_{i=1}^{n} R_{i,p}(\xi)\boldsymbol{P}^k_{h,i}, \qquad \boldsymbol{A}^k(\xi) = \sum_{i=1}^{n} R_{i,p}(\xi)\boldsymbol{P}^k_{A,i}, \qquad \boldsymbol{D}^k(\xi) = \sum_{i=1}^{n} R_{i,p}(\xi)\boldsymbol{P}^k_{D,i}, \tag{27}$$

where $k = 1, \ldots, N_{pr}+1$, is an index running over the laminates per control point, and $\boldsymbol{P}^k_{h,i}$ is the thickness of laminate k at control point i. Similarly, $\boldsymbol{P}^k_{A,i}$ and $\boldsymbol{P}^k_{D,i}$ are the membrane and bending stiffness matrices of laminate k at control point i.

3.3. Finite Element model

The finite element model is generated using the geometric model and the material properties, discussed in subsections 3.1 and 3.2, respectively. The blade geometry is discretized in span-wise direction and over the cross-section using two parameters. The first parameter is N_{cr}, which determines the number of elements in chord direction. The second parameter is the aspect ratio of a shell element, defined as $ar = \frac{\Delta S}{\Delta C}$, where ΔS and ΔC are the length of an element in span-wise and chord direction, respectively.

The partition of the cross-section is done separately on the airfoil level, such that any cross-section that is a combination of the base airfoils is also discretized with the same number of elements. The discretization of the blade in span-wise direction is depicted in figure 5, where the cross-section at ξ_{i+1} is calculated by determining ξ_{i+1}, such that

$$\Delta S_i - \int_{\xi_i}^{\xi_{i+1}} J(\xi)d\xi = 0 \tag{28}$$

is satisfied, for $i = 1, \ldots, N_s$, where $\xi_{N_s} = 1$. Equation 28 is solved numerically for ξ_{i+1} using the *matlab fminbnd* function.

The finite element solver *NASTRAN* is used to calculate the structural response of a wind turbine rotor. The finite elements employed to model a wind turbine rotor are the *CQUAD4* elements. The laminate properties may be defined in *NASTRAN* using a combination of *PSHELL* and *MAT2* card. The *PSHELL* card is used to assign the laminate thickness, while the *MAT2* card is used to assign the shell thickness, normalized membrane $\hat{\boldsymbol{A}}$ and bending $\hat{\boldsymbol{D}}$ stiffness properties. The laminate properties, for elements between the cross-sections at ξ_i and ξ_{i+1}, are calculated using equation 27, for $\xi = \frac{1}{2}\left(\xi_i + \xi_{i+1}\right)$.

The *RBE3* card is used to apply the aeroelastic loads, calculated using the low fidelity *aeroelastic* model, to the NASTRAN model and perform static and buckling analysis together with sensitivity analysis. The multipoint connections, used in the *RBE3* card, are defined per cross-section, as shown in figure 5.

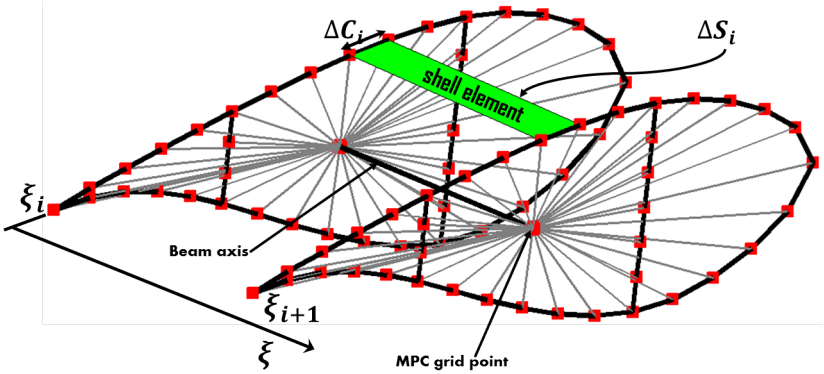

Figure 5. Discretization of the geometry in span wise direction and representation of RBE3 connection

4. AEROELASTIC MODEL

An aeroelastic model is presented, where geometrically exact beam model is used to calculate the non-linear displacements while the Blade Element Momentum theory is employed to calculate the aerodynamic loads. In addition, the centrifugal loads are also taken into account during the aeroelastic analysis.

4.1. Structural Model

The wind turbine blade is modelled using the geometrically exact beam theory [26] together with the Timoshenko beam model. The Timoshenko beam model removes the need to determine the location of the shear center, making it useful for *composite* optimization.

The internal force resultant and tangent stiffness matrix are respectively, the first and second variation of the strain energy with respect to the generalized coordinates. The generalized coordinates are the displacement of the beam axis and its rotation. The strain energy is expressed in terms of the strain measures and the stress and stress-couple resultants,

$$U = \frac{1}{2}\int_0^L \left(\boldsymbol{\gamma}^t \boldsymbol{N} + \boldsymbol{\kappa}^t \boldsymbol{M}\right) dx, \tag{29}$$

where the stress and stress-couple resultants($\boldsymbol{N}$and$\boldsymbol{M}$) are related to the strain measures($\boldsymbol{\gamma}$and$\boldsymbol{\kappa}$), through the Timoshenko stiffness matrix as

$$\boldsymbol{F} = \boldsymbol{S}\boldsymbol{\epsilon}, \tag{30}$$

where $\boldsymbol{S}$ is the six by six Timoshenko stiffness matrix[27] and $\boldsymbol{F}$ is the generalized stress resultant composed of the stress and stress-couple resultants as $\boldsymbol{F} = \begin{Bmatrix} \boldsymbol{N} & \boldsymbol{M} \end{Bmatrix}$. The the generalized strain measure $\boldsymbol{\epsilon}$ is composed of the translational and rotational strain measures as $\boldsymbol{\epsilon} = \begin{Bmatrix} \boldsymbol{\gamma} & \boldsymbol{\kappa} \end{Bmatrix}$.

Starting from the Reissner-Simo beam theory [28], the translational and rotational strain measures, with respect to the body-attached frame at a given cross-section are related to the beam configuration($\boldsymbol{u}, \boldsymbol{R}$) through the equations

$$\boldsymbol{\gamma} = \boldsymbol{\Lambda}_0^t \left(\boldsymbol{R}^t \boldsymbol{u}' + \left(\boldsymbol{R}^t - \boldsymbol{I}\right)\boldsymbol{r}_0'\right) \qquad \text{and} \qquad \hat{\boldsymbol{\kappa}} = \boldsymbol{\Lambda}_0^t \boldsymbol{R}^t \boldsymbol{R}' \boldsymbol{\Lambda}_0, \tag{31}$$

where $\hat{\boldsymbol{\kappa}}$ is the skew symmetric matrix of the rotational strain measure $\boldsymbol{\kappa}$ and $(\prime)$ denotes derivative with respect to the arc-length x. The displacement of the beam axis is denoted by $\boldsymbol{u}$, while $\boldsymbol{R}$ is the rotation matrix, which maps the orthonormal base vectors from the initial configuration($\boldsymbol{g}_{0,i}$) to the deformed configuration($\boldsymbol{g}_i$).

The rotation matrix and its variation with respect to the generalized coordinates is expressed in quaternion representation of rotations. More on parametrization of rotation using quaternions can be found in [29, 30, 31, 32]. The generalized load resultant and the tangent stiffness matrix are given as

$$\boldsymbol{f} = \int_0^L \boldsymbol{\epsilon}\boldsymbol{S}\frac{\partial \boldsymbol{\epsilon}}{\partial \boldsymbol{q}} ds \qquad \text{and} \qquad \boldsymbol{K} = \int_0^L \left(\frac{\partial \boldsymbol{\epsilon}^t}{\partial \boldsymbol{q}}\boldsymbol{S}\frac{\partial \boldsymbol{\epsilon}}{\partial \boldsymbol{q}} + \boldsymbol{\epsilon}^t \boldsymbol{S}\frac{\partial^2 \boldsymbol{\epsilon}}{\partial \boldsymbol{q}\partial \boldsymbol{q}}\right) ds \tag{32}$$

where $\boldsymbol{q}$ is a vector, composed of the generalized displacements and rotations. Isogeometric formulation is employed to evaluate equation 32, where Non-Uniform Rational B-splines are used as basis functions [].

4.2. Centrifugal load

Rotating bodies experience centrifugal effects. These forces are non existent in inertial frame of reference, however in rotating frame, the centrifugal effects are seen as inertial loads [33]. These inertial effects can be decomposed into centrifugal force and Coriolis force. Only the centrifugal effect is considered for current static aeroelasticity. The kinetic energy of a beam is defined as

$$T = \frac{1}{2}\int_M |\boldsymbol{v}_l|^2 \, dm \tag{33}$$

where $\boldsymbol{v}_l$ is the velocity of the differential mass dm with respect to the rotating frame. Assuming only static blade deformations, $\boldsymbol{v}_l$ is related to the position vector of a particle in rotating frame as, $\boldsymbol{v}_l = \omega \hat{\boldsymbol{e}}_\omega \boldsymbol{r}_l$, where ω and $\hat{\boldsymbol{e}}_\omega$ are respectively, the magnitude and direction, in skew symmetric notation, of the angular velocity of the blade.

The position vector $\boldsymbol{r}_l$ of a mass particle is expressed as $\boldsymbol{r}_l = \boldsymbol{r}_b + \boldsymbol{\Lambda}\boldsymbol{r}_p$, where $\boldsymbol{r}_b$ is the position vector of the beam axis and $\boldsymbol{r}_p$ is the position vector of mass particle with respect to the body-attached base vectors $\boldsymbol{\Lambda}_0$. Assuming small rotations, the beam axis and the body-attached base vectors are parametrized as

$$\boldsymbol{r}_b = \boldsymbol{r}_{b,0} + \boldsymbol{u} \qquad \text{and} \qquad \boldsymbol{\Lambda} = \left(\boldsymbol{I} + \hat{\boldsymbol{\theta}}\right)\boldsymbol{\Lambda}_0, \tag{34}$$

where $\boldsymbol{r}_{b,0}$ and $\boldsymbol{\Lambda}_0$ are the initial beam axis and body-attached base vectors, respectively. The displacement and rotation of the beam axis are denoted by $\boldsymbol{u}$ and $\boldsymbol{\theta}$ respectively.

Using the fact that $dm = \rho dA ds$, where dA and ds are the differential area and arc-length, the kinetic energy is expressed as double integral along the cross-section and the arch-length as,

$$T = \frac{1}{2}\int_0^L \int_A |\boldsymbol{v}_g|^2 \, \rho dA ds, \tag{35}$$

where ρ is the material density. The generalized centrifugal force and stiffness are the first and second variation of the kinetic energy with respect to the generalized coordinates $\left(\boldsymbol{q} = \{\boldsymbol{u}, \boldsymbol{\theta}\}^t\right)$,i.e

$$\boldsymbol{f}_{ct} = \int_0^L \int_A \frac{\partial |\boldsymbol{v}_g|^2}{\partial \boldsymbol{q}} \rho dA ds, \qquad \text{and} \qquad \boldsymbol{K}_{ct} = \int_0^L \int_A \frac{\partial^2 |\boldsymbol{v}_g|^2}{\partial \boldsymbol{q} \partial \boldsymbol{q}} \rho dA ds. \tag{36}$$

4.3. Aerodynamic Model

The Blade Element Momentum(BEM) theory with tip loss correction, described in [34], is used to calculate at the integration point ξ, the aerodynamic force and moment vector per unit length. The BEM model requires as input among others: the blade radius $r(\xi)$, chord $c_a(\xi)$, twist $\theta_a(\xi)$ and the polar data of the airfoil $\boldsymbol{A}_{af}(\xi)$.

Starting from the expression for the deformed beam axis

$$\boldsymbol{r}(\xi) = \sum_{i=1}^{n} R_{i,p}(\xi)(\boldsymbol{P}_{ri} + \boldsymbol{u}_i), \tag{37}$$

where $\boldsymbol{u}_i$ is the unknown displacement at control point i and $\boldsymbol{P}_{ri}$ is the initial beam axis at control point i, the radius along the blade span is calculated as

$$r(\xi) = r_h + \|\boldsymbol{r}(\xi) \times \boldsymbol{e}_3\|, \tag{38}$$

where r_h is the hub radius and $\boldsymbol{e}_3$ is a component of the inertial frame shown in figure 2.

For flexible blades or blades with initially curved beam axis, the undisturbed airflow sees a different airfoil shape than the structural airfoil shape, as shown in figure 6. This requires that the airfoil polar data needs to be calculated per integration point ξ. This increases the computational time, thus not useful for fast analysis or optimization. Other possibility is to use a correction on the chord and twist by projecting the airfoil shape defined in the structural frame unto the aerodynamic frame and calculating the chord and twist of the projected airfoil shape, as shown in figure 7. To apply this correction, it is assumed that the chord and twist vary slowly.

The chord c_s and twist θ_s at the parametric point ξ are define as

$$c_s(\xi) = \sum_{j=1}^{m}\sum_{i=1}^{n} R_{i,p}(\xi)\boldsymbol{C}_{i,j} \qquad \text{and} \qquad \theta_s(\xi) = \sum_{i=1}^{n} R_{i,p}(\xi)\boldsymbol{P}_{\theta,i}. \tag{39}$$

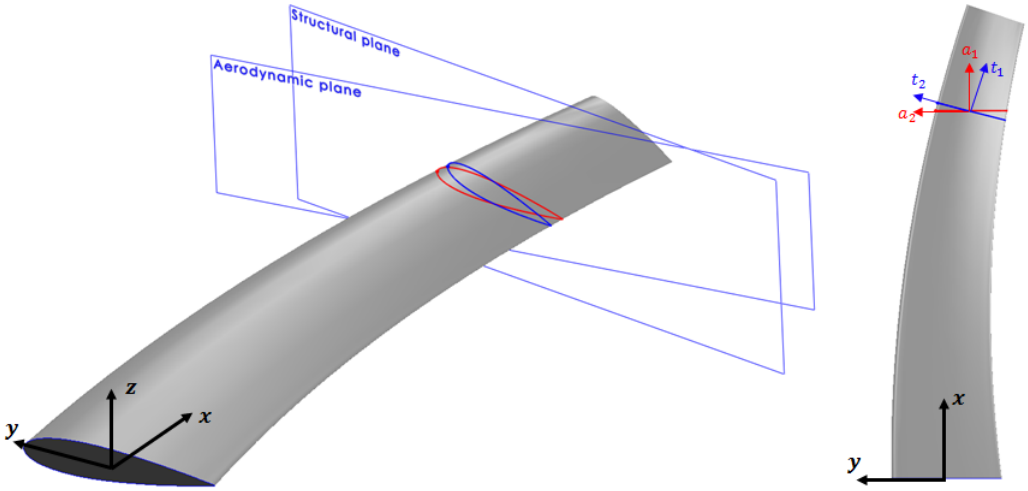

Figure 6. 3D and top view of a curved and twisted blade where $\boldsymbol{a}_i$ are base vectors of the aerodynamic frame and $\boldsymbol{t}_i$ are base vectors of the structural frame

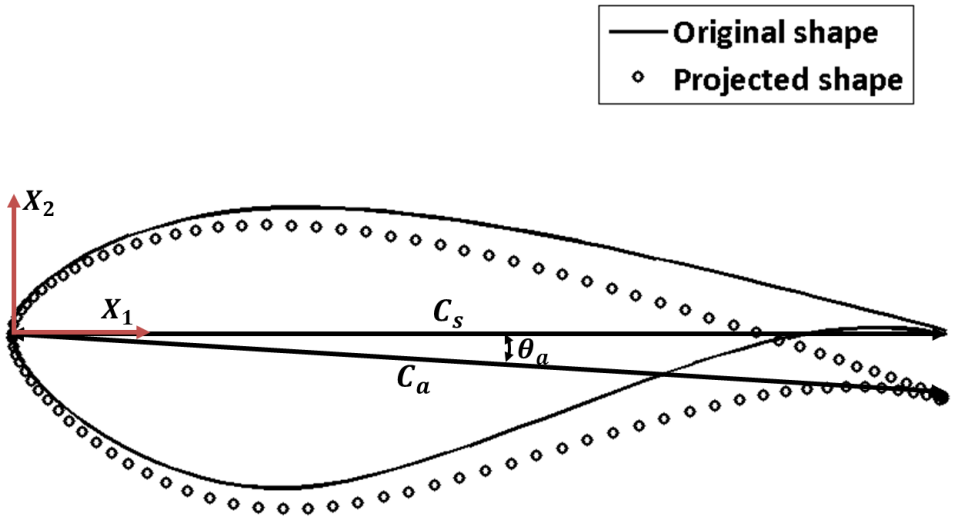

Figure 7. Projection of a cross-section from the structural plane unto the aerodynamic plane along $\boldsymbol{a}_1$

As mentioned earlier, the chord and twist given in equation 39 are corrected for the flexibility of the blade, first by projecting the airfoil shape defined in the structural plane to the aerodynamic plane(see figure 7). The cross-sectional shape of a blade at ξ may be expressed with respect to the body-attached structural frame $\boldsymbol{\Lambda}_s(\xi)$ or the aerodynamic frame $\boldsymbol{\Lambda}_a(\xi)$ as

$$\boldsymbol{\Lambda}_s(\xi)\boldsymbol{r}_s = \boldsymbol{\Lambda}_a(\xi)\boldsymbol{r}_a, \tag{40}$$

where $\boldsymbol{t}_i$, for $i = 1, \ldots, 3$, are the base vectors of the structural frame $\boldsymbol{\Lambda}_s$, defined as

$$\boldsymbol{t}_1 = \boldsymbol{R}\bar{\boldsymbol{t}}_1, \qquad \boldsymbol{t}_2 = \boldsymbol{R}\big(\cos(\theta_s)\bar{\boldsymbol{t}}_2 - \sin(\theta_s)\bar{\boldsymbol{t}}_3\big), \qquad \text{and} \qquad \boldsymbol{t}_3 = \boldsymbol{R}\big(\sin(\theta_s)\bar{\boldsymbol{t}}_2 + \cos(\theta_s)\bar{\boldsymbol{t}}_3\big), \tag{41}$$

where

$$\bar{\boldsymbol{t}}_1 = \frac{1}{J(\xi)}\frac{d\boldsymbol{r}}{d\xi}, \qquad \bar{\boldsymbol{t}}_2(\xi) = \bar{\boldsymbol{t}}_1(\xi) \times \boldsymbol{e}_2, \qquad \text{and} \qquad \bar{\boldsymbol{t}}_3(\xi) = \bar{\boldsymbol{t}}_2(\xi) \times \bar{\boldsymbol{t}}_1(\xi), \tag{42}$$

and $\boldsymbol{R}$ is the matrix representation of rotation. The vectors $\boldsymbol{a}_i$,for $i = 1, \ldots, 3$, are the base vectors of the aerodynamic frame $\boldsymbol{\Lambda}_a$, defined as

$$\boldsymbol{a}_1 = \frac{1}{\|\boldsymbol{r}(\xi) \times \boldsymbol{e}_3\|} \boldsymbol{I}_1^t \boldsymbol{r}(\xi), \qquad \boldsymbol{a}_2 = \frac{1}{\|\boldsymbol{r}(\xi) \times \boldsymbol{e}_3\|} \boldsymbol{I}_2^t \boldsymbol{r}(\xi), \qquad \text{and} \qquad \boldsymbol{a}_3 = \boldsymbol{e}_3, \tag{43}$$

where $\boldsymbol{I}_1 = \big[\boldsymbol{e}_1, \boldsymbol{e}_2, \boldsymbol{0}\big]$ and $\boldsymbol{I}_1 = \big[\boldsymbol{e}_2, \boldsymbol{e}_1, \boldsymbol{0}\big]$. The vectors $\boldsymbol{r}_s$ and $\boldsymbol{r}_a$ are the co-ordinates of the cross-section with respect to the structural and aerodynamic frame, respectively. Since $\boldsymbol{e}_1^t \boldsymbol{r}_s = 0$, $\boldsymbol{r}_{a,1}$ is expressed as

$$\boldsymbol{r}_{a,1} = -\frac{\boldsymbol{t}_1^t \boldsymbol{a}_2}{\boldsymbol{t}_1^t \boldsymbol{a}_1} \boldsymbol{r}_{a,2} - \frac{\boldsymbol{t}_1^t \boldsymbol{a}_3}{\boldsymbol{t}_1^t \boldsymbol{a}_1} \boldsymbol{r}_{a,3}, \tag{44}$$

where $\boldsymbol{r}_{a,i}$, for $i = 1, \ldots, 3$, is the ith component of $\boldsymbol{r}_a$. The shape of the cross-section, defined in the structural plane, is projected unto the aerodynamic plane along $\boldsymbol{a}_1$, such that

$$\bar{\boldsymbol{r}}_a = \boldsymbol{P} \bar{\boldsymbol{r}}_s, \tag{45}$$

where

$$\boldsymbol{P} = \bar{\boldsymbol{I}}^t \boldsymbol{\Lambda}_s^t \bar{\boldsymbol{\Lambda}}_a, \tag{46}$$

and $\bar{\boldsymbol{I}} = \big[\boldsymbol{e}_2, \boldsymbol{e}_3\big]$. $\bar{\boldsymbol{r}}_s$ is the co-ordinate of the airfoil shape in the structural plane, whereas $\bar{\boldsymbol{r}}_a$ is the co-ordinate of the projected airfoil shape in the aerodynamic plane. Components of $\bar{\boldsymbol{\Lambda}}_a = \big[\bar{\boldsymbol{a}}_2, \bar{\boldsymbol{a}}_3\big]$ are calculated as

$$\bar{\boldsymbol{a}}_2 = \boldsymbol{a}_2 - \frac{\boldsymbol{t}_1^t \boldsymbol{a}_2}{\boldsymbol{t}_1^t \boldsymbol{a}_1} \boldsymbol{a}_1 \qquad \text{and} \qquad \bar{\boldsymbol{a}}_3 = \boldsymbol{a}_3 - \frac{\boldsymbol{t}_1^t \boldsymbol{a}_3}{\boldsymbol{t}_1^t \boldsymbol{a}_1} \boldsymbol{a}_1. \tag{47}$$

The chord, corrected for blade flexibility and/or initially curved beam axis, is calculated using the projected matrix $\boldsymbol{P}$ as

$$c_a = c_s \sqrt{\bar{\boldsymbol{e}}_1^t \boldsymbol{P}^t \boldsymbol{P} \bar{\boldsymbol{e}}_1}, \tag{48}$$

where $\bar{\boldsymbol{e}}_1 = \{1, 0\}^t$ and c_s is the structural chord.

The corrected twist θ_a is calculated as

$$\theta_a = \sin^{-1}\left(\tfrac{c_s}{c_a} \bar{\boldsymbol{e}}_2^t \boldsymbol{P} \bar{\boldsymbol{e}}_1\right) \frac{180}{\pi}, \tag{49}$$

where $\bar{\boldsymbol{e}}_2 = \big\{0, 1\big\}^t$.

The polar data of the airfoil shape at the parametric point ξ is calculated from the polar data of the base airfoils as,

$$\boldsymbol{A}_{af}(\xi) = \frac{1}{c_s(\xi)} \sum_{j=1}^{m} \sum_{i=1}^{n} R_{i,p}(\xi) \boldsymbol{C}_{i,j} \boldsymbol{A}_{paf,j}, \tag{50}$$

where $\boldsymbol{A}_{paf}(\xi)$ is a matrix containing the $C_l, C_d,$ and C_m data, for a range of α, of airfoil j in a given pool.

Wind shear is taken into account when calculating the aerodynamic load on a single blade(see figure 2). The wind speed, of all blades, at $r(\xi)$ is sampled for a range of, user supplied, azimuth angle and hub height wind speed U, using the power law defined in the IEC guidelines []. The average aerodynamic force and moment at ξ is calculated as

$$\bar{\boldsymbol{f}}(\xi) = \sum_{i=1}^{N_w} w_i \boldsymbol{f}_i(\xi), \qquad \text{and} \qquad \bar{\boldsymbol{m}}(\xi) = \sum_{i=1}^{N_w} w_i \boldsymbol{m}_i(\xi), \tag{51}$$

where N_w is the number of sampled azimuth positions, w_i is the weight of the aerodynamic load calculated at the azimuth position ϕ_i,such that $\sum_{i=1}^{N_w} w_i = 1$.

4.4. Aerostructural coupling

In most cases of structural design or optimization of wind turbine blades, the aerodynamic loads are applied as fixed loads, meaning the aerodynamic loads are not dependent on the structural deformation. This assumption is valid for stiff structures. For flexible structures however, the aerodynamic loads are dependent on the structural deformation and vice-versa. The Aeroelastic solution is obtained by equating the internal loads with external loads, expressed mathematically

as,

$$\boldsymbol{R} = \boldsymbol{f}_{int}\left(\boldsymbol{q}, \boldsymbol{u}\right) - \boldsymbol{f}_{ext}\left(\boldsymbol{q}, \boldsymbol{u}\right) = \boldsymbol{0}, \tag{52}$$

Where $\boldsymbol{R}$ is the residual vector, $\boldsymbol{q}$ is the generalized displacement and rotation vector, and u is the mean wind speed. The generalized internal and external load vectors($\boldsymbol{f}_{int}$, and $\boldsymbol{f}_{ext}$) are defined as,

$$\boldsymbol{f}_{int} = \boldsymbol{f}_{s} - \omega^2 \boldsymbol{K}_{cs}\boldsymbol{q}, \qquad \text{and} \qquad \boldsymbol{f}_{ext} = \boldsymbol{f}_{a} + \omega^2 \boldsymbol{f}_{cs}, \tag{53}$$

where ω is the rotational speed, and $\boldsymbol{f}_{s}$ and $\boldsymbol{f}_{cs}$ are the generalized structural and centrifugal load resultants given in equations 32 and 36, respectively. The generalized load resultant for the aerodynamic loads($\boldsymbol{f}_{a}$) is given as,

$$\boldsymbol{f}_{a} = \int_0^1 \left(\frac{\partial \boldsymbol{u}^t}{\partial \boldsymbol{q}} \boldsymbol{\Lambda}_a \bar{\boldsymbol{f}} + \frac{\partial \boldsymbol{\theta}^t}{\partial \boldsymbol{q}} \boldsymbol{\Lambda}_a \bar{\boldsymbol{m}} \right) J d\xi. \tag{54}$$

Aeroelastic equilibrium condition is achieved when the residual of equation 52 converges to zero. To simulate the operation of pitch regulated wind turbine rotors, an additional equilibrium equation is added, namely the power after the rated wind speed is limited to the rated power supplied by the user. An additional general coordinate, namely the pitch angle is added to the generalized displacement and rotation vector $\boldsymbol{q}$ as, $\boldsymbol{q}_\theta = \left\{\boldsymbol{q}^t, \theta\right\}^t$. Therefore, the augmented equilibrium equations are as follows,

$$\boldsymbol{f}_{int}\left(\boldsymbol{q}_\theta, \boldsymbol{u}\right) - \boldsymbol{f}_{ext}\left(\boldsymbol{q}_\theta, \boldsymbol{u}\right) = \boldsymbol{0}, \qquad \text{and} \qquad P\left(\boldsymbol{q}_\theta, \boldsymbol{u}\right) - P_{rated} = 0, \tag{55}$$

where P_{rated} and P are the rated power and the power calculated at wind speed u.

The non-linear aeroelastic equilibrium is calculated by dividing the wind speed u into a given number of steps, controlled by the parameter λ. At a given (fraction of)wind speed λu, a prediction of the equilibrium point for the next wind speed is made by linearising the equilibrium equation 55 around the current equilibrium point. Followed by a correction phase, keeping λ constant and varying the generalized coordinates $\boldsymbol{q}_\theta$ until the equations in 55 are satisfied.

5. HIGH-FIDELITY STRUCTURAL ANALYSIS

The finite element solver *NASTRAN* is used to calculate high-fidelity structural response using the shell model of the wind turbine blade. The aeroelastic loads, including the centrifugal loads, calculated on the low-fidelity model, are applied as static loads on the *NASTRAN* model using the *RBE3* card described in section 3.3. The aeroelastic force and moment vectors per unit length are interpolated on the *RBE3* elements using the virtual work principle, given as

$$\boldsymbol{f}_{RBE3} = \int_0^1 \boldsymbol{N}^t(\xi)\boldsymbol{f}_{interp}(\xi)J(\xi)d\xi \qquad \text{and} \qquad \boldsymbol{m}_{RBE3} = \int_0^1 \boldsymbol{N}^t(\xi)\boldsymbol{m}_{interp}(\xi)J(\xi)d\xi, \tag{56}$$

where,

$$\boldsymbol{N}(\xi) = \begin{bmatrix} n_1(\xi) & 0 & 0 & n_2(\xi) & 0 & 0 \\ 0 & n_1(\xi) & 0 & 0 & n_2(\xi) & 0 \\ 0 & 0 & n_1(\xi) & 0 & 0 & n_2(\xi) \end{bmatrix}, \tag{57}$$

and n_1 and n_2 are linear shape functions of the two grid points connected to an *RBE3* element. The definition of the jacobian $J(\xi)$ is given in equation 14. The force $\boldsymbol{f}_{interp}(\xi)$ and moment $\boldsymbol{m}_{interp}(\xi)$ vectors per unit length are linear interpolation of the aeroelastic loads calculated using the low fidelity model, i.e. $\boldsymbol{f}_{interp}(\xi) = \Psi(\bar{\boldsymbol{f}}(\xi_{ae}), \xi)$ and $\boldsymbol{m}_{interp}(\xi) = \Psi(\bar{\boldsymbol{m}}(\xi_{ae}), \xi)$, where Ψ is the *Matlab interp1* function, used to interpolate the aeroelastic loads sampled at ξ_{ae}.

Aside from the analysis of the structural responses, *NASTRAN* is also used to asses the sensitivity of the structural responses with respect to the design variables. To achieve this, the design optimization solution sequence is used with the execution control statement *SOL 200*, while setting the parameter *END=SENS* of the *NASTRAN DSAPRT* card to halt *NASTRAN* analysis after generating the responses with their sensitivities. *NASTRAN* employs, depending on the type of responses, two methods of sensitivity analysis, i.e direct or adjoint method [35]. However, for the responses requested in the present method, *NASTRAN* employs solely the direct method in calculating the sensitivities. The total derivative of a response r with respect to a design variable x is calculated as

$$\frac{\partial r}{\partial x} = \frac{\partial r}{\partial \boldsymbol{u}} \frac{\partial \boldsymbol{u}}{\partial x}, \tag{58}$$

where $\boldsymbol{u}$ is the displacement solution, obtained from the static equilibrium equation $\boldsymbol{K}\boldsymbol{u} = \boldsymbol{f}$.

The partial derivative of $\boldsymbol{u}$ with respect to x is given as

$$\boldsymbol{K}\frac{\partial \boldsymbol{u}}{\partial x} = \frac{\partial \boldsymbol{f}}{\partial \boldsymbol{u}} - \frac{\partial \boldsymbol{K}}{\partial \boldsymbol{u}}\boldsymbol{u}, \tag{59}$$

where the right hand side of the above equation is denoted as a pseudo load vector $\boldsymbol{f}_p$. The pseudo load vector is composed of two terms, one of which is the derivative of the applied load $\boldsymbol{f}$ with respect to the design variable x. The sensitivity of the applied load $\frac{\partial \boldsymbol{f}}{\partial \boldsymbol{u}}$ needs to be provided explicitly to *NASTRAN*.

During sensitivity analysis, *NASTRAN* calculates per design variable x, using finite difference, $\Delta\boldsymbol{u}$ as follows

$$\boldsymbol{K}\Delta\boldsymbol{u} = -\left(\Delta\boldsymbol{K}\boldsymbol{u} - \tfrac{\partial \boldsymbol{f}}{\partial \boldsymbol{u}}\Delta x\right), \tag{60}$$

where the differential Δx is calculated inside *NASTRAN* as $\Delta x = DELBx_0$, for $DELB = 0.001$. The first term on the right hand side of equation 60 is calculated by *NASTRAN*, whereas the second term is provided to *NASTRAN* using the *DMAP* programming language [36].

The first term of the pseudo load vector defined in equation 60($\Delta\boldsymbol{K}\boldsymbol{u}$) is calculated by the module *PSLGDV*, as such the contribution of the design dependent load $\boldsymbol{f}(x)$ in calculating $\Delta\boldsymbol{u}$ is taken into account by adding $-\frac{\partial \boldsymbol{f}}{\partial \boldsymbol{u}}\Delta x$ to the variable *EGK*, which contains $\Delta\boldsymbol{K}\boldsymbol{u}$. *NASTRAN* uses central or forward finite difference to calculate the derivative of the stiffness matrix $\boldsymbol{K}$ with respect to the design variable x.

The responses and sensitivities calculated by *NASTRAN* are extracted by requestion the response vector *R1VALRG* and the sensitivity matrix *DSM2*, using alter commands described in [36].

6. RESPONSE DEFINITION

The present method defines two types of responses. The first type of responses are those calculated by the low-fidelity aeroelastic tool. Starting from the aerodynamic force and moment at the root of a single blade, calculated for a hub-height wind speed U as,

$$\boldsymbol{f}_r(U) = \int_0^1 \bar{\boldsymbol{f}}(\xi, U)J(\xi, U)d\xi \qquad \text{and} \qquad \boldsymbol{m}_r = \int_0^1 \left(\bar{\boldsymbol{m}}(\xi, U) + \boldsymbol{r}(\xi, U) \times \bar{\boldsymbol{f}}(\xi, U)\right) J(\xi, U)d\xi, \tag{61}$$

the total thrust and torque are

$$r_{th}(U) = B\boldsymbol{e}_3^t\boldsymbol{f}_r(U) \qquad \text{and} \qquad r_{to}(U) = B\boldsymbol{e}_3^t\boldsymbol{m}_r(U), \tag{62}$$

respectively, where B is the number of blades, $\boldsymbol{r}$ is the deformed beam axis, J is the Jacobian of the deformed beam axis, and $\boldsymbol{e}_3 = \left\{0, 0, 1\right\}^t$. The tip deflection and the aerodynamic power are given by

$$\delta_{tip}(U) = \sum_{i=1}^{n} R_{i,p}(\xi = 1)\boldsymbol{u}_i(U) \qquad \text{and} \qquad P(U) = \omega(U)r_{to}(U), \tag{63}$$

respectively, where $\boldsymbol{u}_i(U)$ is the displacement vector of the beam axis at control point i. Since the aeroelastic analysis is performed for finite (hub-height) wind speeds, the maximums of $r_{th}(U)$,$r_{to}(U)$,$\delta_{tip}(U)$,$P(U)$ are calculated for each response by bracketing, with respect to the wind speed U, till the maximum is found.

The second type of responses are calculated using the finite element solver *NASTRAN*. The membrane stress resultants $\boldsymbol{N} = \left\{N_x, N_y, N_{xy}\right\}^t$ of element i from the high-fidelity shell model of the blade is given by

$$\boldsymbol{N}_i = \frac{1}{2}h_i\left(\boldsymbol{\sigma}_i^u + \boldsymbol{\sigma}_i^l\right), \tag{64}$$

where h_i is the shell thickness of element i and $\boldsymbol{\sigma}_i^u$ and $\boldsymbol{\sigma}_i^l$ are the membrane stresses at the top and bottom side, in shell thickness direction, of element i, requested in *NASTRAN* analysis using the *DRESP1* card [37]. In addition to the stress responses, *NASTRAN* is used to calculate the shell buckling load factor λ, which is also extracted from the *NASTRAN* analysis using the *DRESP1* card.

7. VALIDATION/VERIFICATION OF THE AERODYNAMIC/AEROELASTIC MODEL

The aerodynamic module of the present method is validated using the experimental results of the EU-sponsored project *MEXICO*. For this project, a three bladed wind turbine rotor with a diameter of $4.5m$ is tested in a wind tunnel with dimensions $9.5 \times 9.5m^2$. The rotor blade consists of the following profiles: circular from 0 to 20% span, *DU91-W2-250* from 20 to 45% span, *RISO* from 55 to 65% span, *NACA 64418* from 70 to 100% span. Detailed description of the experimental campaign and the dimensions of the wind turbine rotor can be found in [38]. The normal and tangential force distribution, calculated using the present method, is compared with experimental data of the MEXICO project, for tip speed ratio $\lambda = 6.7$, wind speed $U = 15m/s$ and rotational speed $\omega = 44.5rad/s$. The current method calculates the aerodynamic loads at 54 integration points. Figures 8a and 8b show the comparison of the normal and tangential force distribution for the pitch angles $\theta = -2.3\,\text{deg}$ and $0.7\,\text{deg}$, respectively.

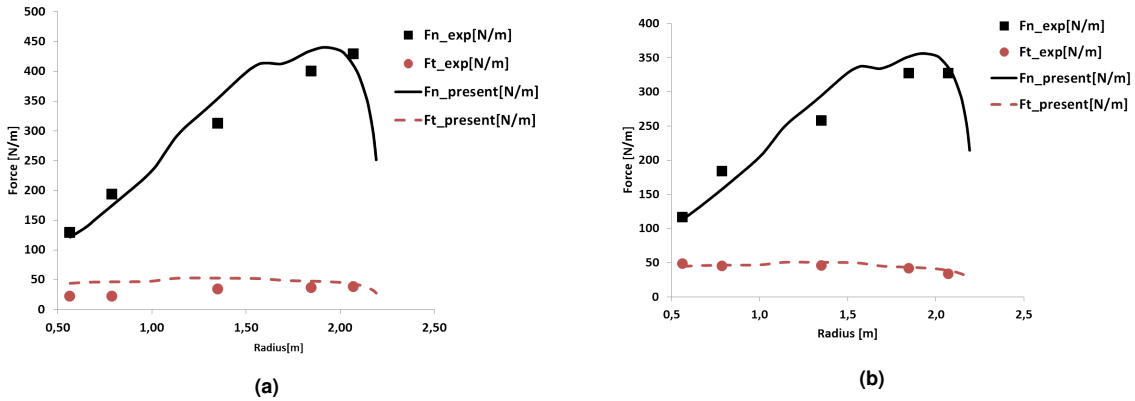

Figure 8. Comparison of the axial force F_n and tangential force F_t distribution with the MEXICO experimental results at wind speed of $15m/s$ and pitch angles: (8a) $-2.3\,\text{deg}$ and (8b) $0.7\,\text{deg}$.

From figures 8a and 8b, the present method predicts the normal and tangential forces quite well towards the root of the blade. The tip loads are predicted quite well with the current model, for both the pitch angles of $-2.3\,\text{deg}$ and $0.7\,\text{deg}$. There is difference in the tangential force between the experimental data and the present method. The experimental data for the tangential force is not accurate, since pressure data is used to calculate the force distribution, which doesn't account for viscous forces. The tangential force distribution is dependent on the viscous force, thus is less accurately accounted by the experimental data. The present model predicts the aerodynamic loads quite well, and is thus capable of predicting the aerodynamic loads on wind turbines with sufficient accuracy.

The aeroelastic code is verified against *FAST*[39] and the commercially available aeroelastic code *GH Bladed* [40]. A quasi-steady analysis is performed on the NREL 5MW reference turbine [22]. The blade geometry is generated using B-spline basis functions of degree 3 and knot spans of 20. The aerodynamic loads are calculated at 60 integration point. Detailed description of the turbine and blade properties can be found in [22].

The parameters used as representative of aeroelastic behaviour of the turbine are: power, thrust, (flap-wise) root bending moment, and the (flap-wise) tip deflection. The comparison of the parameters mention above, is shown in figures 9a to 10b for wind speeds $5m/s$ till $18m/s$. The power curve, shown in figure 9a, agrees quite well between the three methods. The thrust calculated by the present method and GH Bladed match(see figure 9b), while there is a noticeable difference between the results obtained by FAST and the present method. This is also observed for the (flap-wise) root bending moment 10a and tip deflection 10b. The reason for this discrepancy could be caused due to the implementation of a wake model in FAST, which is not the case for the other two methods.

7.1. Swept blade

Bend-twist coupled blades are used in stall regulated wind turbines for power and load regulation [17]. Bend-twist coupled blades can be designed with the use of composite materials, where off axis fibres are used to induce bend-twist coupling [41]. It is more costly to manufacture blades with off axis fibres. In addition, fatigue is an issue for these type of blades, where stress concentrations occur due to curving or ending of angled fibres [42]. Another method would be designing swept blades, where the sweep distribution along the blade span induces additional moment that twists the blade further [42].

The present method allows for changing the blade design, such that these novel methods in designing bend-twist coupled blades can be performed more easily, which is demonstrated by assessing the performance of the Sandia $30m$ STAR

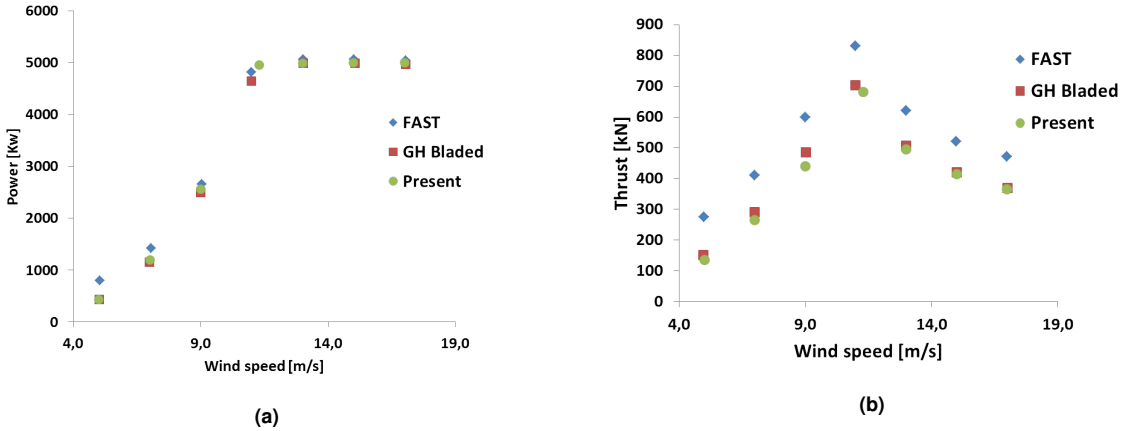

Figure 9. Comparison of: power(9a) and thrust(9b), between FAST,GH Bladed and the present method, for the NREL 5MW machine.

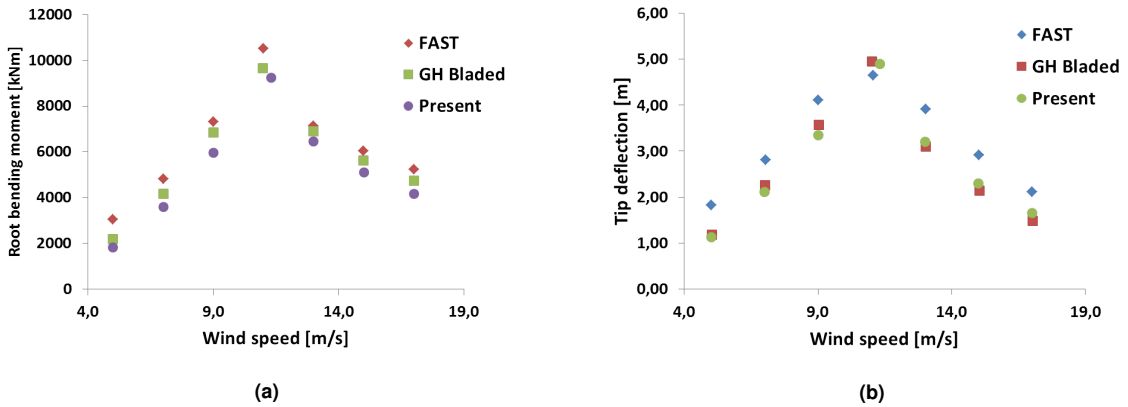

Figure 10. Comparison of: (flap-wise) root bending moment (10a) and (flap-wise) tip deflection, between FAST,GH Bladed and the present method, for the NREL 5MW machine.

blade[23]. The blade geometry is generated using B-spline basis functions of degree 3 and 11 control points, with the resulting *knot vector* $\Xi = \left\{0, 0, 0, \frac{1}{4}, \frac{1}{2}, \frac{3}{4}, 1, 1, 1\right\}$. The base airfoils used to generate the cross-sectional shape are [43]: *circular*, *S818*, *S827*, *S828*. A single spar at 35% chord point is modelled. The control point values of the blade planform and the beam axis, derived from [42], are shown in table I. The leading and trailing edge, together with the shear webs, are made of sandwich laminates, where the core is made of foam and the face sheets and the spar caps are made of glass fibres, with the material properties given in [44]. A quasi-isotropic laminate with the layup $[-45, 45, 0, 90]_{symmetric}$, is used for the face sheets, whereas the laminate thickness distribution is derived from [44]. The finite element model of the blade is shown in figure 11.

The aeroelastic load on the wind turbine is calculated for a hub height wind speed of $19m/s$ and rotational speed of $12.2rpm$. Figure 12a shows the design chord and twist distribution together with the chord and twist distribution, that account for the aeroelastic effect. From figure 12a it is evident that the twist distribution, corrected for aeroelastic effect, is different from the structural twist towards the tip of the blade, with maximum difference of $0.5deg$. There is negligible difference in chord distribution between the structural chord and the chord distribution corrected for aeroelastic effect. The change in twist distribution results in different angle of attack(AoA) distribution as shown in figure 12b. This has an effect on the normal and tangential force distribution along the blade span, shown in figure 13. In this figure, there is a difference between the loads calculated with and without taking the aeroealstic effect into account. The tangential load distribution in particular shows a significant difference starting from $20m$ til the blade root, with a maximum difference of 5%. This difference is also observed for the axial force distribution, but less pronounced than for the tangential force distribution.

The present method also calculates the stress distribution along the blade span together with the buckling load factor. Figure 14a shows the stress resultant, calculated using equation 64, where the aeroealstic load distribution along the blade span are calculated for the wind speed of $19m/s$. In figure 14b, the first three buckling load factors λ, together with their buckling modes, are shown for the aeroelastic load calculated at $19m/s$.

Table I. Planform data of a swept blade derived from [44]

CP	Twist(deg)	Chord(m)	R_x(m)	R_y(m)	R_z(m)
1	29.5	1.66	0	0	0
2	29.5	1.66	1.6	0	0
3	19.5	2.48	3.3	0	0
4	13	2.75	6.7	0	0
5	8.8	2.42	10.1	0	0
6	6.2	2.12	13.5	0.1	0
7	4.4	1.84	16.9	0.1	0
8	3.1	1.56	20.3	0.2	0
9	1.9	1.29	23.6	0.4	0
10	0.8	1.02	27	0.8	0
11	0	0.76	30.4	1.5	0

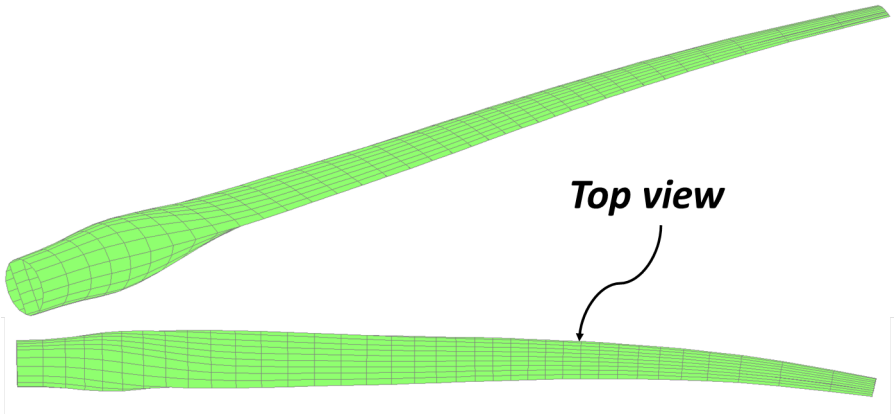

Figure 11. Swept wind turbine blade

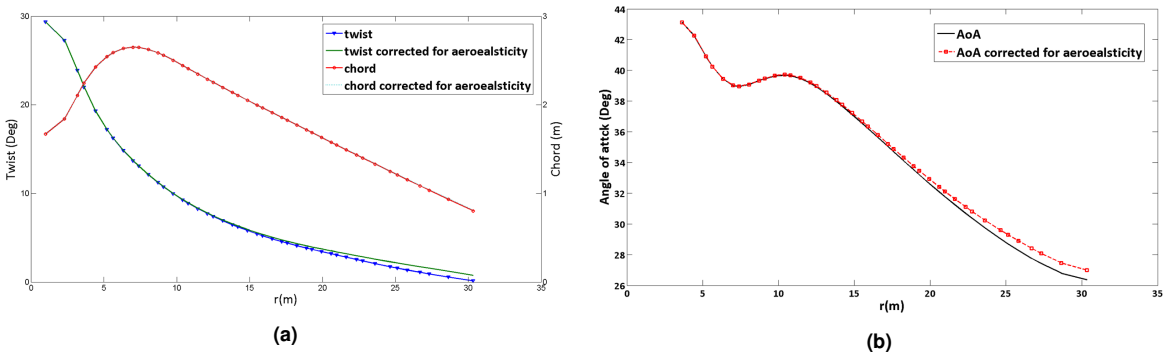

Figure 12. 12a Chord and twist distribution of the swept blade and 12b distribution of the angle of attack(AoA) at $19m/s$

8. CONCLUSION

An isogeometric framework is presented for parametrizing a wind turbine rotor blade and multi-fidelity approach for wind turbine rotor analysis. The aeroelastic loads are determined using a low-fidelity model. This low-fidelity model is based on isogeometric approach to model both the structural and aerodynamic properties, because of its suitability for shape and size optimization. The structural properties are determined using a geometrically exact beam model and a standard Blade Element Momentum(BEM) method is used to calculate the aerodynamic loads. In addition, the aerodynamic loads calculated using BEM theory are modified to account for change in the blade shape during shape optimization or for very flexible blade undergoing large deformation. The cross-sectional properties of the blade, needed for the beam model, are

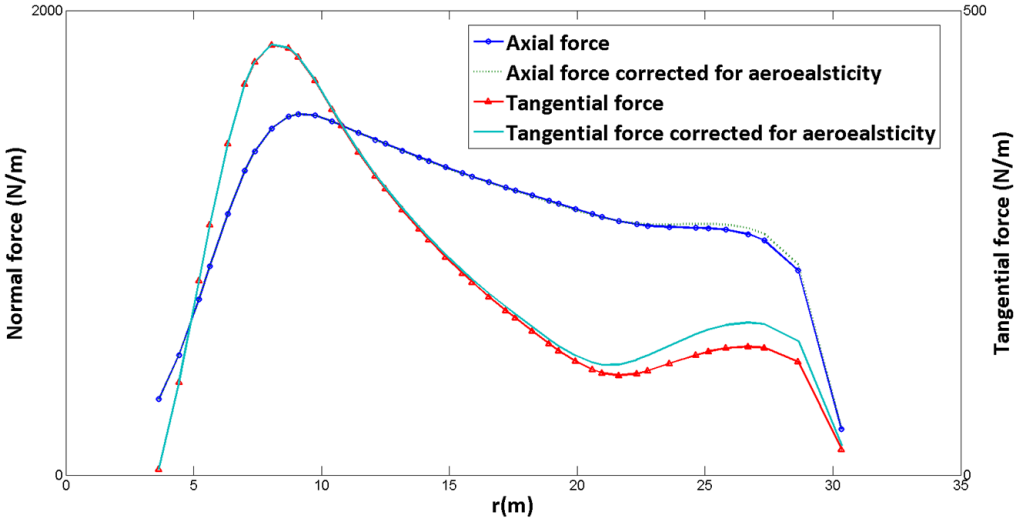

Figure 13. Axial and tangential force along the blade span at $19m/s$

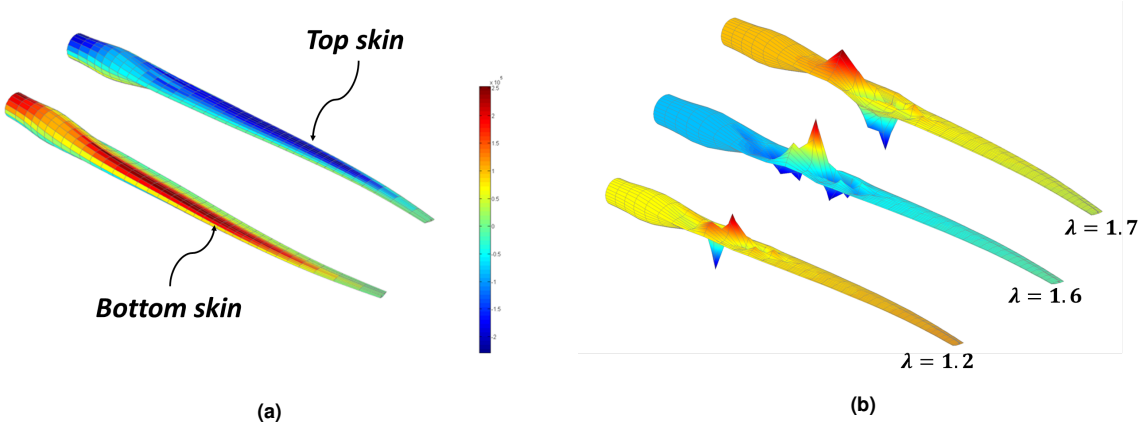

Figure 14. 14a Average stress resultant distribution calculated at $19m/s$ and 14b the first three buckling loads

determined using an in-house tool that generates the cross-sectional stiffness properties with all possible couplings for thin-walled, multi-cell, open or closed cross-sections with anisotropic properties.

The aeroelastic loads are applied in Nastran as static loads to a shell model of the blade and both the stress response and buckling response are extracted. In addition, sensitivity of the aeroelastic responses to the design variables are available, such that this framework can also be used to optimize the rotor blade. Furthermore, the capabilities of Nastran are extended such that design dependent loads can be applied, resulting in correct sensitivities of Nastran responses with respect to the design variables.

The aerodynamic module is validated against the experimental data of the EU-sponsored *MEXICO* project. A comparison between the experimental results and the present method is performed for the normal and tangential force distribution, for the pitch angles of $-2.3deg$ and $0.7deg$, showing a good match between experiment and the present method.

The aeroelastic module is verified using the NREL $61.5m$ rotor blade as a baseline for comparison. The power, thrust, flap-wise root bending moment and the tip deflection, calculated for a range of mean wind speeds, is compared between the present method, *FAST* and *GH Bladed*, showing a good agreement with results from GH *GH Bladed* and a small difference between the results from *FAST*, which can be attributed to the implementation of a wake model which is not the case for the present method and *GH Bladed*. Finally, the capability of the present method in designing and analysing non-conventional blades is demonstrated by investigating the aeroelastic characteristics of the Sandia $30m$, *STAR* blade.

It can be concluded that this framework is suitable for preliminary analysis and optimization of wind turbine rotor blades, using both the geometric and material parameters as design variables.

REFERENCES

1. S.-E. Thor, P. Weis-Taylor, Long-term research and development needs for wind energy for the time frame 2000–2020, Wind Energy 5 (1) (2002) 73–75.
2. J. Schepers, J. Heijdra, D. Foussekis, S. Øye, R. Rawlinson Smith, M. Belessis, K. Thomsen, T. Larsen, I. Kraan, B. Visser, et al., Verification of European wind turbine design codes, VEWTDC: final report, Netherlands Energy Research Foundation ECN, 2002.
3. T. Van Engelen, Control design based on aero-hydro-servo-elastic linear models from turbu (ecn), in: Proceeding of the European wind energy conference, Milan, Italy, 2007.
4. P. Passon, M. Kühn, State-of-the-art and development needs of simulation codes for offshore wind turbines, in: Copenhagen Offshore Wind 2005 Conference and Expedition Proceedings, 2005, pp. 26–28.
5. A. Ahlström, Aeroelastic simulation of wind turbine dynamics, Ph.D. thesis, Department of Mechanics, Royal Institute of Technology Stockholm (2005).
6. C. Lindenburg, H. Snel, Aero-elastic stability analysis tools for large wind turbine rotor blades, in: Proceedings of the 2003 European Wind Energy Conference and Exhibition, Vol. 6, European Wind Energy Association Madrid, Spain, 2003.
7. P. Zhang, S. Huang, Review of aeroelasticity for wind turbine: Current status, research focus and future perspectives, Frontiers in Energy 5 (4) (2011) 419–434.
8. M. Jureczko, Pawlak, Optimisation of wind turbine blades, Journal of Materials Processing Technology 167 (2) (2005) 463–471.
9. E. Benini, A. Toffolo, Optimal design of horizontal-axis wind turbines using blade-element theory and evolutionary computation, Journal of Solar Energy Engineering 124 (4) (2002) 357–363.
10. G. Eke, J. Onyewudiala, Optimization of wind turbine blades using genetic algorithm, Global Journal of Researches in Engineering 10 (7).
11. M. Grujicic, G. Arakere, B. Pandurangan, V. Sellappan, A. Vallejo, M. Ozen, Multidisciplinary design optimization for glass-fiber epoxy-matrix composite 5 mw horizontal-axis wind-turbine blades, Journal of Materials Engineering and Performance 19 (8) (2010) 1116–1127.
12. W. Xudong, W. Z. Shen, W. J. Zhu, J. N. Sørensen, C. Jin, Shape optimization of wind turbine blades, Wind Energy 12 (8) (2009) 781–803.
13. P. Fuglsang, H. Madsen, Optimization method for wind turbine rotors, Journal of Wind Engineering and Industrial Aerodynamics 80 (1) (1999) 191–206.
14. P. Fuglsang, K. Thomsen, Site-specific design optimization of 1.5–2.0 mw wind turbines, Journal of solar energy engineering 123 (4) (2001) 296–303.
15. P. Fuglsang, C. Bak, J. Schepers, B. Bulder, T. Cockerill, P. Claiden, A. Olesen, R. van Rossen, Site-specific design optimization of wind turbines, Wind Energy 5 (4) (2002) 261–279.
16. P. Veers, D. Lobitz, G. Bir, Aeroelastic tailoring in wind-turbine blade applications, Tech. rep., Sandia National Labs., Albuquerque, NM (United States) (1998).
17. A. Maheri, S. Noroozi, J. Vinney, Application of combined analytical/fea coupled aero-structure simulation in design of wind turbine adaptive blades, Renewable Energy 32 (12) (2007) 2011–2018.
18. W. De Goeij, M. Van Tooren, A. Beukers, Implementation of bending-torsion coupling in the design of a wind-turbine rotor-blade, Applied Energy 63 (3) (1999) 191–207.
19. S. Larwood, M. Zuteck, Swept wind turbine blade aeroelastic modeling for loads and dynamic behavior, AWEA windpower (2006) 1–17.
20. J. A. Cottrell, T. J. Hughes, Y. Bazilevs, Isogeometric analysis: toward integration of CAD and FEA, John Wiley & Sons, 2009.
21. M.-C. Hsu, I. Akkerman, Y. Bazilevs, High-performance computing of wind turbine aerodynamics using isogeometric analysis, Computers & Fluids 49 (1) (2011) 93–100.
22. J. M. Jonkman, S. Butterfield, W. Musial, G. Scott, Definition of a 5-MW reference wind turbine for offshore system development, National Renewable Energy Laboratory Golden, CO, 2009.
23. T. D. Ashwill, Sweep-twist adaptive rotor blade: final project report., Tech. rep., Sandia National Laboratories (2010).
24. L. A. Piegl, W. Tiller, The NURBS book, Springer, 1995.
25. R. N. Goldman, T. Lyche, Knot insertion and deletion algorithms for B-spline curves and surfaces, Vol. 36, SIAM, 1993.
26. J. C. Simo, L. Vu-Quoc, A geometrically-exact rod model incorporating shear and torsion-warping deformation, International Journal of Solids and Structures 27 (3) (1991) 371–393.
27. E. A. Ferede, M. M. Abdalla, Cross-sectional modelling of thin-walled composite beams, in: Proceedings of the 55th AIAA/ASMe/ASCE/AHS/SC Structures, Structural Dynamics, and Materials Conference, 2014.

28. J. Simo, L. Vu-Quoc, A three-dimensional finite-strain rod model. part ii: Computational aspects, Computer methods in applied mechanics and engineering 58 (1) (1986) 79–116.
29. B. K. Horn, Closed-form solution of absolute orientation using unit quaternions, JOSA A 4 (4) (1987) 629–642.
30. J. Schmidt, H. Niemann, Using quaternions for parametrizing 3-d rotations in unconstrained nonlinear optimization., in: VMV, Vol. 1, 2001, pp. 399–406.
31. J. Stuelpnagel, On the parametrization of the three-dimensional rotation group, SIAM review 6 (4) (1964) 422–430.
32. R. Mukundan, Quaternions: From classical mechanics to computer graphics, and beyond, in: Proceedings of the 7th Asian Technology conference in Mathematics, 2002, pp. 97–105.
33. M. Berzeri, A. A. Shabana, A finite element study of the geometric centrifugal stiffening effect, Tech. rep., DTIC Document (1999).
34. T. Burton, D. Sharpe, N. Jenkins, E. Bossanyi, Wind energy handbook, John Wiley & Sons, 2001.
35. G. J. Moore, MSC/NASTRAN Design Sensitivity and Optimization User's Guide, MSC, 1994.
36. M. Robinson, Programming DMAP in MSC.Nastran Direct Matrix Abstract Programming, Mark Robinson, 2012.
37. R. S. Lahey, M. P. Miller, M. Reymond, Msc/nastran reference manual, version 68, The MacNeal-Schwendler Corporation.
38. J. Schepers, K. Boorsma, T. Cho, S. Gomez-Iradi, P. Schaffarczyk, A. Jeromin, W. Shen, T. Lutz, K. Meister, B. Stoevesandt, et al., Final report of iea task 29, mexnext (phase 1): Analysis of mexico wind tunnel measurements, Wind Energy 2013 (2014) 2012.
39. J. M. Jonkman, M. L. Buhl Jr, Fast users guide, Golden, CO: National Renewable Energy Laboratory.
40. E. Bossanyi, Gh bladed theory manual, GH & Partners Ltd.
41. W. De Goeij, M. Van Tooren, A. Beukers, Implementation of bending-torsion coupling in the design of a wind-turbine rotor-blade, Applied Energy 63 (3) (1999) 191–207.
42. M. D. Zuteck, Adaptive blade concept assessment: curved planform induced twist investigation, Sandia National Laboratories, 2002.
43. J. L. Tangler, D. M. Somers, Nrel airfoil families for hawts, Tech. rep., National Renewable Energy Lab., Golden, CO (United States) (1995).
44. B. R. Resor, Definition of a 5mw/61.5 m wind turbine blade reference model, Albuquerque, New Mexico, USA, Sandia National Laboratories, SAND2013-2569 2013.